Enhancement of the Walker limit by bulk Dzyaloshinskii-Moriya interaction

Mei Li ®, Bin Xi, Yongjun Liu,* and Jie Lu ®†

College of Physics Science and Technology, Yangzhou University, Yangzhou 225002, People's Republic of China

In this work, the effects of bulk Dzyaloshinskii-Moriya interactions (BDMIs) on magnetic domain walls in noncentrosymmetric chiral magnets are investigated. For static walls, their chirality is jointly determined by BMDI strength and the hard-easy ratio. When external magnetic fields or electronic currents are applied, the Walker limit is considerably enhanced by BDMIs. Domain walls can acquire high enough steady-flow velocity that they are more easily liberated from various blocking mechanisms and thus can serve as fast carriers of information. In addition, modifications of the BDMI strength and hard-easy ratio to the walls' drifting velocity far beyond Walker breakdown are presented. Our findings open possibilities for the development and optimization of future magnetic nanodevices with high performance and better environmental friendliness.

I. INTRODUCTION

Magnetic topological solitons are isolated spin textures with spatial localization and topological protection. The thorough understanding of their statics and dynamics in various magnetic heterostructures (MHs) is the basis for the invention and optimization of new magnetic recording and processing devices. Recently, discussions about chiral magnetic solitons stabilized by the Dzyaloshinskii-Moriya interaction (DMI) have become extraordinarily active. The most common examples are chiral domain walls (DWs) [1–6], skyrmions/antiskyrmions [7–12], and bimerons [13–17]. Historically, the bulk DMI (BDMI) was proposed first. As an antisymmetric exchange coupling, it includes an odd term of the spatial gradient of magnetization [18]. From the microscopic point of view, BDMI comes from the generalization of Anderson's superexchange interaction in the presence of spin-orbit coupling [19]. Experimentally, it was first proposed to reside in chiral magnets with noncentrosymmetric B20 structure [7,8,20,21]. The noncollinear magnetic structures observed recently in several Heusler compounds also suggest its possible existence therein [22,23].

Over the last decade, heavy-metal substrates have been widely used in MHs [24–38]. In these setups, the interfacial DMI (IDMI) and spin Hall and Rashba spin-orbit torques emerge together. They complicatedly affect the static chirality of walls in the ferromagnetic central layer and their motion under external driving forces [34–40]. We call these systems IDMI-MHs for short. Alternatively, little attention has been paid to MHs with central layers made of magnets with BDMI and normal nonmagnetic substrates (called BDMI-MHs). Compared with the well-studied IDMI-MHs, BDMI-MHs have the advantages of weaker toxicity and lower cost. They are excellent candidates for future magnetic nanodevices with greater environmental friendliness and high cost-effectiveness.

On the other hand, the variety of magnetic materials with BDMI is not very rich. To acquire high performance of DWs in BDMI-MHs, we need to explore other adjustment methods in addition to tuning BDMI strength. The simplest, but efficient, way is to change the cross-section shape of the central layer, thus varying the "hard-easy ratio" κ (total anisotropy in the hard axis over that in the easy one). Therefore, a systematic investigation of static chirality and dynamical behaviors of DWs in BDMI-MHs with a tunable BDMI strength and hard-easy ratio should be of great interest and importance.

In the present work we focus on strip-shaped BDMI-MHs with perpendicular magnetic anisotropy (PMA). Once nucleated, DWs are driven to move longitudinally by either out-of-plane magnetic fields or in-plane electronic currents. In principle, both steady and precessional flows emerge. Their dividing point, the Walker limit, will be enhanced by BDMI, thus allowing DWs to acquire high enough steady-flow velocities. When far beyond the Walker breakdown, κ provides another dimension of effectively modifying DW dynamics. The rest of this paper is organized as follows. In Sec. II the system setup and its modelization are briefly introduced. Then the chirality of static walls is investigated in Sec. III. After that, the field-driven and current-driven dynamics of DWs are studied in Secs. IV and V, respectively. Finally, further discussions and a conclusion are provided in the last section.

II. MODEL AND METHODS

The magnetic free-energy density $\mathscr{E}_0$ of the chiral magnet in a MH (see Fig. 1) includes four parts: the exchange part $\mathscr{E}_{\mathrm{ex}} = A(\nabla \mathbf{m})^2$ (A and $\mathbf{m}$ are the exchange stiffness and magnetization unit vector); the Zeeman part $\mathscr{E}_{\mathrm{Z}} = -\mu_0 M_s \mathbf{m} \cdot \mathbf{H}_a$, with the total external field $\mathbf{H}_a$ and the saturation magnetization M_s; the anisotropy part $\mathscr{E}_{\mathrm{ani}} = (\mu_0 M_s^2/2)(-k_{\mathrm{E}} m_z^2 + k_{\mathrm{H}} m_y^2)$, where k_{E} (k_{H}) is the total (crystalline plus shape) anisotropy coefficient in the easy (hard) axis; and the BDMI

*yjliu@yzu.edu.cn
†lujie@yzu.edu.cn
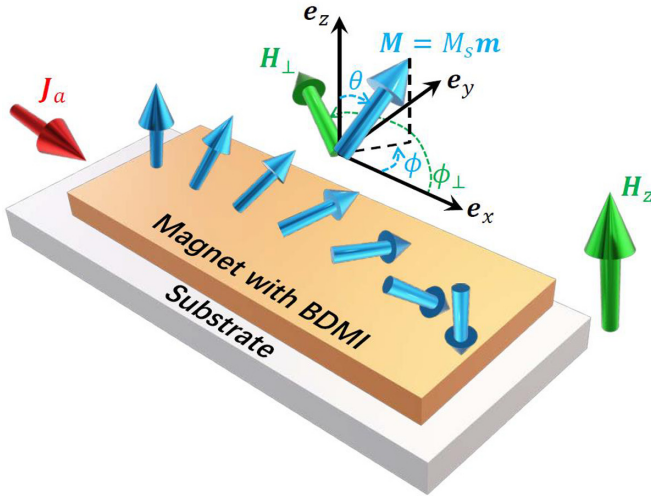
FIG. 1. A strip-shaped MH in which a chiral magnet with BDMI and PMA is prepared on a nonmagnetic substrate. The magnetization $\mathbf{M} = M_s\mathbf{m}$ is fully described by its polar and azimuthal angles (θ and ϕ). An $\uparrow\downarrow$ wall is driven to move in the x direction by either an out-of-plane field $\mathbf{H}_z$ or an in-plane current density $\mathbf{J}_a$. In the meantime, an in-plane bias field, $\mathbf{H}_\perp = H_\perp(\cos\phi_\perp \mathbf{e}_x + \sin\phi_\perp \mathbf{e}_y)$, is applied to further manipulate the wall's behavior.

contribution $\mathscr{E}_b = D_b\mathbf{m}(\mathbf{r}) \cdot [\nabla \times \mathbf{m}(\mathbf{r})]$, with D_b being the BDMI strength [41]. In this work we consider PMA, which is common in chiral magnets.

Under out-of-plane magnetic fields and in-plane currents, the Lagrangian $\mathscr{L}$ of this chiral magnet is

$$\frac{\mathscr{L}}{\mu_0 M_s^2} = -\frac{\cos\theta}{\gamma M_s}\frac{\partial\phi}{\partial t} - \frac{B_J\phi}{\gamma M_s}\frac{\partial\cos\theta}{\partial(\hat{\mathbf{J}}\cdot\mathbf{r})} - \frac{\mathscr{E}_0}{\mu_0 M_s^2}, \quad (1)$$

with the dissipative functional

$$\frac{\mathscr{F}}{\mu_0 M_s^2} = \frac{\alpha}{2\gamma M_s}\left\{\left[\frac{\partial}{\partial t} - \frac{\beta B_J}{\alpha}\frac{\partial}{\partial(\hat{\mathbf{J}}\cdot\mathbf{r})}\right]\mathbf{m}\right\}^2 \quad (2)$$

describing various damping processes [42–47]. Here $\theta(\mathbf{r}, t)$ and $\phi(\mathbf{r}, t)$ are the polar and azimuthal angles of $\mathbf{m}(\mathbf{r}, t)$, respectively. α is the damping constant, and β is the nonadiabatic spin-transfer torque coefficient. $\gamma = \mu_0\gamma_e$, with μ_0 and γ_e being the vacuum permeability and electron gyromagnetic ratio, respectively. $B_J = \mu_B P J_a/(eM_s)$, in which μ_B is the Bohr magneton and e (>0) is the absolute electron charge. J_a (with unit vector $\hat{\mathbf{J}}$) is the current density flowing longitudinally through the chiral magnet with polarization P.

The magnetization dynamics of the chiral magnet is described by the Lagrangian-Rayleigh equation,

$$\frac{d}{dt}\left(\frac{\delta\mathscr{L}}{\delta\dot{X}}\right) - \frac{\delta\mathscr{L}}{\delta X} + \frac{\delta\mathscr{F}}{\delta\dot{X}} = 0, \quad (3)$$

where an overdot means $\partial/\partial t$ and X is any related coordinate. To explore collective behaviors, the Lagrangian-based collective coordinate model is used, which needs a preset ansatz of walls. For strip-shaped MHs, we adopt the Walker ansatz [48,49]

$$\ln\tan\frac{\vartheta}{2} = \eta\frac{x - q(t)}{\Delta}, \quad \phi = \varphi(t), \quad (4)$$

where q, Δ, and φ are the wall center position, wall width, and in-plane magnetization angle, respectively. $\eta = +1$ (-1) is the topological wall charge that corresponds to the $\uparrow\downarrow$ ($\downarrow\uparrow$) wall. For the narrow-strip geometry shown in Fig. 1, the $\mathbf{e}_x$ and $\mathbf{e}_y$ axes respectively indicate the longitudinal (L) and transverse (T) directions. By setting $X = q, \varphi, \Delta$ and integrating along the longitudinal direction ($\int_{-\infty}^{+\infty} dx$), the following closed dynamical equations are obtained:

$$(1 + \alpha^2)\dot{\varphi} = \gamma H_z + (\alpha - \beta)\frac{\eta B_J}{\Delta} - \frac{\alpha\pi\gamma}{2}\left[\frac{k_H M_s}{\pi}\sin 2\varphi\right.$$

$$\left. + H_\perp\sin(\varphi - \phi_\perp) + \frac{\eta D_b\cos\varphi}{\mu_0 M_s\Delta}\right],$$

$$\dot{q} = -\frac{\eta\Delta}{\alpha}\dot{\varphi} + \frac{\eta\Delta\gamma}{\alpha}H_z - \frac{\beta}{\alpha}B_J,$$

$$\frac{\alpha\pi}{6\gamma_0}\frac{\dot{\Delta}}{\Delta} = \frac{2A}{\pi\mu_0 M_s\Delta^2} - \frac{M_s}{\pi}(k_E + k_H\sin^2\varphi)$$

$$+ H_\perp\cos(\varphi - \phi_\perp). \quad (5)$$

These are all we need to proceed with our investigation.

III. STATIC WALL CHIRALITY

When $H_z = 0$ and $J_a = 0$, the wall remains static. In the absence of in-plane bias fields, the total magnetic energy is $E_0/S = \int_{-\infty}^{+\infty}\mathscr{E}_0[\mathbf{M}]dx = 2A/\Delta + \mu_0 M_s^2\Delta(k_E + k_H\sin^2\varphi) + \eta\pi D_b\sin\varphi$, where S is the cross-sectional area of the chiral magnet. For static walls, the last equation in Eq. (5) provides $\Delta = \Delta_0(1 + \kappa\sin^2\varphi)^{-1/2}$, with $\Delta_0 = \sqrt{2A/(\mu_0 k_E M_s^2)}$ and $\kappa \equiv k_H/k_E$ being the hard-easy ratio. Consequently, $E_0/S = 2[2A\mu_0 M_s^2(k_E + k_H\sin^2\varphi)]^{1/2} + \eta\pi D_b\sin\varphi$. When BDMI is absent, either $\varphi = 0$ or $\varphi = \pi$ provides the minimum of E_0. Thus, the wall takes a Néel-type profile, and no chirality is preferred. As D_b appears, the minimization operation of E_0/S provides

$$\frac{(E_0)_{\min}}{\pi S D_0} = \begin{cases} \sqrt{\left(1 + \frac{1}{\kappa}\right)\frac{1}{\kappa} - \left(\frac{D_b}{D_0}\right)^2\frac{1}{\kappa}} & \text{at } \sin\varphi_0 = -\eta\,\text{sgn}(D_b)\sqrt{\frac{(D_b/D_0)^2}{(1+\kappa) - \kappa(D_b/D_0)^2}} \text{ for } |D_b| < D_0, \\ \left(1 + \frac{1}{\kappa}\right) - \frac{|D_b|}{D_0} & \text{at } \sin\varphi_0 = -\eta\,\text{sgn}(D_b) \text{ for } |D_b| \geqslant D_0, \end{cases} \quad (6)$$

with $D_0 \equiv (2M_s\sqrt{2A\mu_0 k_E}/\pi)(\kappa/\sqrt{1 + \kappa})$ and sgn indicating the sign function. This means under finite BDMI ($|D_b| < D_0$), the wall is a mixture of Néel and Bloch types and thus shows a certain chirality preference through nonzero $\langle m_y\rangle$. For sufficiently large BDMI ($|D_b| \geqslant D_0$), chiral Bloch walls emerge.

This process is shown in Fig. 2, where $\eta = +1$ and $D_b < 0$ are selected.

When finite out-of-plane fields and/or in-plane currents are applied, Eq. (5) implies that there should be two dynamical modes: the steady-flow (precessional-flow) mode for small
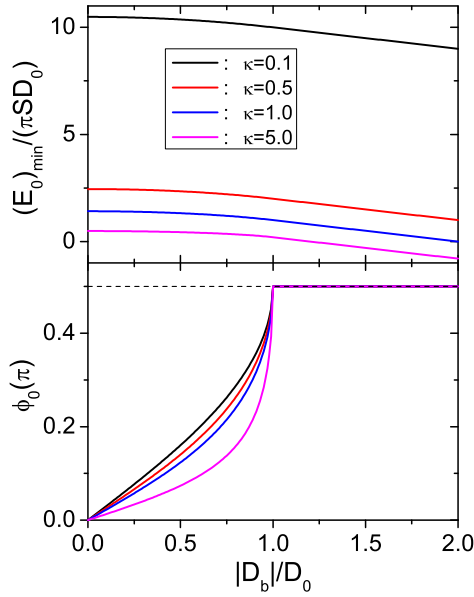
FIG. 2. Evolution of (a) the minimum total magnetic energy and (b) the corresponding in-plane angle of chiral DWs as BDMI increases. Four typical hard-easy ratios κ are presented. For a given κ, there exists a critical BDMI strength D_0. When $|D_b| < D_0$ ($\geqslant D_0$), the wall shows partial (full) chirality.

(large) driving factors. The dividing point is the Walker field or Walker current density, which should be manipulated by BDMI and κ. In the following two sections, field- and current-driven dynamics of DWs will be respectively investigated.

IV. FIELD-DRIVEN DYNAMICS

A. Walker field enhancement by BDMI

First, we define several quantities for further usage: the anisotropy field in the easy axis $H_K = k_E M_s$, the original Walker field $H_W^0 = \alpha \kappa H_K/2$, the BDMI effective field strength $H_b^0 = D_b/(\mu_0 M_s \Delta_0)$, and the dimensionless coefficient $b = \eta \pi H_b^0/H_K$. Now DWs are driven by out-of-plane magnetic field $H_z \mathbf{e}_z$. In the absence of an in-plane bias field $\mathbf{H}_\perp$, the steady-flow mode requires $\dot{\varphi} = 0$ and $\dot{\Delta} = 0$, which lead to

$$\frac{H_z}{H_W^0} = f(\varphi) \equiv \frac{b}{\kappa} \cos\varphi \sqrt{1 + \kappa \sin^2\varphi} + \sin 2\varphi. \quad (7)$$

For fixed b and κ, once $|f(\varphi)|_{\max}$ is found for $\varphi \in [0, 2\pi)$, the new Walker field then reads $H_W = H_W^0 |f(\varphi)|_{\max}$.

Since $f(b, \varphi) = f(-b, \varphi + \pi)$, the sign of b does not affect $|f(\varphi)|_{\max}$. Without loss of generality, we set $b > 0$. In real MHs κ is generally on the order of 10^{-2}–10^0. The explicit form of $|f(\varphi)|_{\max}$ was obtained analytically and is given in Appendix A due to its length. Based on it, the modified Walker fields H_W in units of $H_W^0 (= \alpha \kappa H_K/2)$ and $\alpha H_K/2$ are plotted in Figs. 3(a) and 3(b), respectively. The corresponding in-plane angle φ_0 where H_W is achieved is provided in Fig. 3(c). We choose $0.02 \leqslant \kappa \leqslant 2$ and $0 \leqslant b \leqslant 2$ as our parameter space, which is common in real MHs.

When BDMI is absent ($b = 0$), $H_W \equiv H_W^0 \propto \kappa$. As BDMI emerges, several interesting things happen. First, under finite
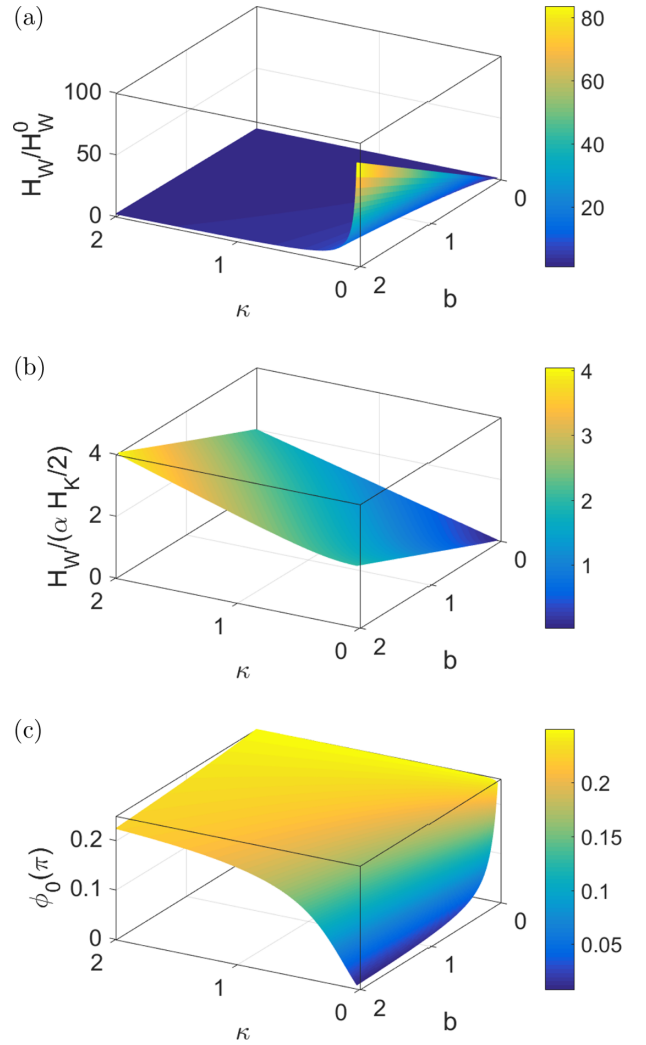
FIG. 3. The BDMI-modified Walker field H_W (a) in units of $H_W^0 = \alpha \kappa H_K/2$ and (b) in units of $\alpha H_K/2$ and (c) the corresponding in-plane angle at which H_W is achieved. All panels are plotted in the parameter space: $\{(\kappa, b) : 0.02 \leqslant \kappa \leqslant 2, 0 \leqslant b \leqslant 2\}$, and the data are calculated based on the results in Appendix A.

BDMI, κ seems to be able to dramatically change the new normalized Walker field [in units of $H_W^0 (= \alpha \kappa H_K/2)$]. For example, at $b = 1$, H_W/H_W^0 increases considerably when κ is below 0.5. In particular, H_W/H_W^0 exceeds 40 when κ decreases to 0.02. When κ gets even smaller, H_W/H_W^0 can be even larger (we neglect this part due to its lack of practicality in real MHs). At the same time, κ also strongly affects the location φ_0 where H_W is achieved as long as $b > 0$: φ_0 varies from $\pi/4$ to 0 as κ decreases from 2 to 0.02. The behaviors of H_W/H_W^0 and φ_0 under small κ can be confirmed by the asymptotic expansion of Eq. (A4) for $\kappa \ll 1$. Direct calculation yields that when $\kappa \ll 1$, $\varphi_0 = \arcsin \tilde{x} \propto \kappa$; thus, Eq. (7) gives $H_W/H_W^0 \to b/\kappa$. This explains the $1/\kappa$ divergence trend for small κ under finite BDMI. On the other hand, recalling $H_W^0 = \alpha \kappa H_K/2$, one finally has

$$H_W \to \frac{\alpha H_K}{2} b = \frac{\alpha \pi |D_b|}{2\mu_0 M_s \Delta_0}, \quad \kappa \ll 1. \quad (8)$$

Obviously, the new Walker limit remains a BDMI-determined finite value even under tiny κ. When $|H_z| < H_W$, the wall velocity reads $\dot{q} = \eta \Delta \gamma H_z / \alpha$, with the wall width $\Delta = \Delta_0 (1 + \kappa \sin^2 \varphi)^{-1/2}$. For small κ, the maximum wall velocity in the steady-flow mode turns out to be

$$v_{\kappa \to 0}^{\max} = \frac{\eta \pi \gamma_e |D_b|}{2 M_s}, \quad \kappa \ll 1, \quad (9)$$

which is independent of (both crystalline and shape) magnetic anisotropy and is solely determined by the BDMI strength and saturation magnetization. For a rough estimation, we choose $\alpha = 0.1$, $|D_b| = 0.5$ mJ/m^2, $M_s = 500$ kA/m, and $\Delta_0 \approx 20$ nm; then $H_W \approx 6.25$ kA/m (≈ 78.5 Oe), and $|v_{\kappa \to 0}^{\max}| \approx 276$ m/s. Obviously, the Walker limit is enhanced by appropriate BDMI strength. Meanwhile, DWs acquire high enough steady-flow velocities that they would easily be liberated from various blocking mechanisms (for example, intrinsic pinning or random impurity potential wells).

In addition, the inclined and almost flat plane in Fig. 3 (b) provides an approximate relationship: $H_W / (\alpha H_K / 2) \approx b + \kappa$. This linear behavior (as well as the "Walker limit enhancement" effect) can be understood as follows. The BDMI energy density leads to the following effective field:

$$\mathbf{H}_b(x) = \frac{2 D_b}{\mu_0 M_s} \left[\left(\frac{\partial m_z}{\partial x} \right) \mathbf{e}_y - \left(\frac{\partial m_y}{\partial x} \right) \mathbf{e}_z \right]$$
$$= -\frac{2 D_b}{\mu_0 M_s} \left[\frac{\eta \sin^2 \vartheta}{\Delta} \mathbf{e}_y + \frac{\eta \sin \vartheta \cos \vartheta \sin \varphi}{\Delta} \mathbf{e}_z \right]. \quad (10)$$

The integration of the z component across the wall region disappears and thus has no effect on wall dynamics. However, the transverse y component always exists in the wall region and contributes a joint action with the existing transverse hard anisotropy field.

B. $\langle \dot{q} \rangle$ under $|H_z| \gg H_W$

When $|H_z|$ exceeds H_W, the Walker breakdown takes place, and the wall falls into the precessional-flow mode. Generally, the breathing wall width ($\dot{\Delta} \neq 0$) has no explicit expression. In the simplest approximation, one has $\Delta = \Delta_0 (1 + \kappa \sin^2 \varphi)^{-1/2}$. By integrating the first equation in Eq. (5) in a full circle, the precessional period T_0 is

$$\bar{\gamma} T_0 = \int_0^{2\pi} \frac{d\varphi / \sqrt{1 + \kappa \sin^2 \varphi}}{\frac{H_z - H_W^0 \sin 2\varphi}{\sqrt{1 + \kappa \sin^2 \varphi}} - \frac{\eta \alpha \pi}{2} H_b^0 \cos \varphi}, \quad (11)$$

where $\bar{\gamma} \equiv \gamma / (1 + \alpha^2)$. Without BDMI, this integration can easily be calculated. As BDMI emerges, Eq. (11) has no explicit form. However, in the high-field limit where $|H_z| \gg \alpha |H_b^0| (H_W^0)$, by using the approximation $(1 - \epsilon)^{-1} \approx 1 + \epsilon + \epsilon^2$, Eq. (11) gives

$$T_0 \approx \frac{2\pi}{\bar{\gamma} H_z} \left[1 + \frac{\alpha^2 \pi^2}{8} \left(1 + \frac{\kappa}{4} \right) \left(\frac{H_b^0}{H_z} \right)^2 + \frac{\alpha^2 \kappa^2}{8} \left(\frac{H_K}{H_z} \right)^2 \right]. \quad (12)$$

Therefore, the time-averaged wall velocity is

$$\langle \dot{q} \rangle_0 = \eta \alpha \Delta_0 \bar{\gamma} H_z \frac{K_0}{2\pi} \left[1 + \frac{\pi^2}{8} \left(1 + \frac{\kappa}{4} \right) \left(\frac{H_b^0}{H_z} \right)^2 + \frac{\kappa^2}{8} \left(\frac{H_K}{H_z} \right)^2 \right], \quad (13)$$

in which K_0 is defined as

$$K_0 = \int_0^{2\pi} \frac{d\varphi}{\sqrt{1 + \kappa \sin^2 \varphi}} = \frac{4}{\sqrt{1 + \kappa}} K\left(\sqrt{\frac{\kappa}{1 + \kappa}} \right), \quad (14)$$

with $K(k) \equiv \int_0^{\pi/2} \frac{d\omega}{\sqrt{1 - k^2 \sin^2 \omega}}$ being the complete elliptic integral of the first kind.

Equation (13) can be reorganized as $c(H_z - H_0)^2 / H_z + d / H_z$, which is exactly the same as Eq. (9) in our early work [50]. Once again, the correctness of our road map on field-driven DW dynamics is verified. Alternatively, when we focus on the effects of BDMI on the walls' drifting velocity, a parabolic $\langle \dot{q} \rangle_0 \sim H_b^0$ relationship emerges which is similar to Eq. (9) in Ref. [33]. Our result here has two advantages: (i) The $H_W^0 \sin 2\varphi$ term has been preserved, leading to the $(H_K)^2$ term which is missing in Ref. [33]. (ii) The dependence of $\langle \dot{q} \rangle_0$ on κ is revealed, which has been totally neglected in most existing studies.

Finally, $v \sim H_z$ curves under $0 < H_z < H_W(b, \kappa)$ and $H_z \gg H_W(b, \kappa)$ for typical (b, κ) combinations are calculated. The main magnetic parameters are the same as those in Sec. IV A. In addition, we set $k_E = 1$, $\eta = +1$, and $b > 0$. Then $H_K = 500$ kA/m, $H_b^0 = 39.8$ kA/m, and $b = 1/4$. $\kappa = 0.1, 0.4$, and 0.7 are selected as three examples to show the effect of the manipulation of κ on DW dynamics. The Walker fields are 7.652, 15.02, and 22.73 kA/m, and the corresponding steady-flow velocities are shown in Fig. 4(a) by black squares, red circles, and blue diamonds, respectively. The three curves coincide with each other very well, indicating the nearly unchanged wall mobility for different κ. In addition, to illustrate high-field behaviors, the walls' drifting velocities under $H_z \in [100, 200]$ kA/m are calculated based on Eq. (13) and plotted in Fig. 4(b). Now κ significantly changes the drifting wall velocity, showing its potential as a new dimension in manipulating DW dynamics.

C. $\langle \dot{q} \rangle \sim H_\perp$ under high H_z

Next the in-plane bias field $\mathbf{H}_\perp = H_\perp (\cos \phi_\perp \mathbf{e}_x + \sin \phi_\perp \mathbf{e}_y)$ is turned on. The Walker field H_W will be further enlarged due to the "pinning" effect of $\mathbf{H}_\perp$ on the in-plane angle φ; however, the explicit form is mathematically hopeless. In this section, we focus on the $\langle \dot{q} \rangle \sim H_\perp$ dependence under sufficiently large H_z where DWs take precessional motion. Similarly, in the simplest approximation the wall width is $\Delta = \Delta_0 (1 + \kappa \sin^2 \varphi)^{-1/2}$. The period for a full circle is similar to that in Eq. (11) except for an additional $-\frac{\alpha \pi}{2} H_\perp \sin(\varphi - \phi_\perp)$ term in the denominator of the integral kernel. In the following we examine two typical cases, namely, longitudinal and transverse in-plane bias fields, to see the behaviors of $\langle \dot{q} \rangle \sim H_\perp$ curves.
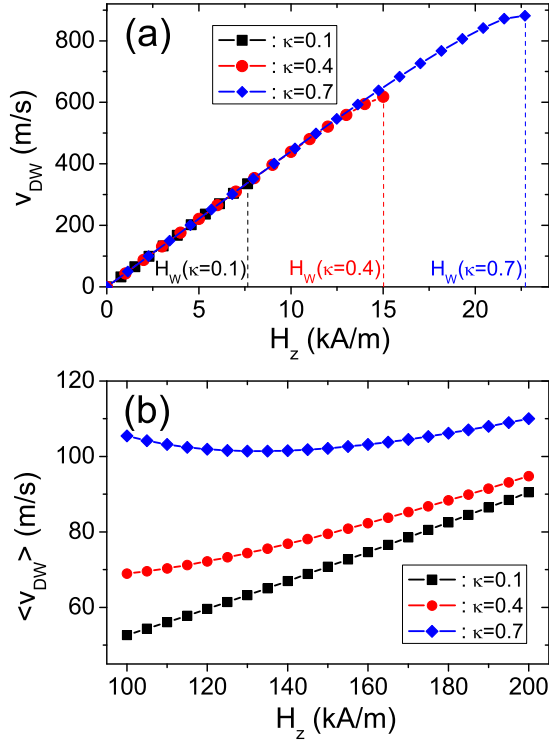
FIG. 4. Field-driven wall velocity in (a) steady-flow and (b) precessional-flow modes for three typical κ: 0.1, 0.4, and 0.7. The magnetic parameters are $\alpha = 0.1$, $|D_b| = 0.5$ mJ/m^2, $M_s = 500$ kA/m, $k_E = 1$, and $\Delta_0 \approx 20$ nm, leading to $b = 1/4$.

For longitudinal in-plane bias fields, $H_\perp = H_x$, and $\phi_\perp = 0$. Under large enough H_z, the new period becomes

$$T_x = T_0 + \frac{2\pi}{\bar{\gamma}H_z}\frac{\alpha^2\pi^2}{8}\left(\frac{H_x}{H_z}\right)^2, \qquad (15)$$

thus leading to a new drifting velocity,

$$\langle \dot{q} \rangle[H_x] = \langle \dot{q} \rangle_0 + \eta\alpha\Delta_0\bar{\gamma}H_z\frac{K_0}{2\pi}\frac{\pi^2}{8}\left(\frac{H_x}{H_z}\right)^2. \qquad (16)$$

For a fixed H_z, this $\langle \dot{q} \rangle \sim H_x$ curve is a parabola going upwards (downwards) with its center located at $H_x = 0$ for $\eta = +1 \, (-1)$.

Alternatively, for transverse in-plane bias fields, $H_\perp = H_y$, and $\phi_\perp = \pi/2$. Similarly, the high-H_z period is

$$T_y = T_0 + \frac{2\pi}{\bar{\gamma}H_z}\frac{\alpha^2\pi^2}{8}\left[\left(\frac{H_y}{H_z}\right)^2 - \frac{\eta K_0}{8\pi}\left(1 + \frac{\kappa}{4}\right)\frac{H_y}{H_z}\frac{H_b^0}{H_z}\right]. \qquad (17)$$

The resulting averaged wall velocity is

$$\langle \dot{q} \rangle[H_y] = \langle \dot{q} \rangle_0 + \eta\alpha\Delta_0\bar{\gamma}H_z\frac{K_0}{2\pi}\frac{\pi^2}{8}\left[\left(\frac{H_y - \delta H_y}{H_z}\right)^2\right.$$
$$\left. - \left(1 + \frac{\kappa}{4}\right)^2\left(\frac{K_0}{2\pi}\right)^2\left(\frac{H_b^0}{H_z}\right)^2\right], \qquad (18)$$

with $\delta H_y = \eta(1 + \frac{\kappa}{4})\frac{K_0}{2\pi}H_b^0$. For a fixed H_z and $\eta = +1 \, (-1)$, the $\langle \dot{q} \rangle \sim H_y$ curve is a parabola going upwards (downwards) with its center located at $H_y = \delta H_y$. For a given BDMI-MH

with fixed κ and a DW with a certain wall charge η, by measuring the $\langle \dot{q} \rangle \sim H_y$ dependence one can extract the BDMI strength D_b from the location of the parabola's center.

In our recent work [45], we constructed a general scheme to identify and quantify BDMI in MHs via precessional flow of DWs under in-plane transverse bias fields. In that scheme, the linearization of trigonometric functions does not lose too many details of the entire circle since walls precess almost evenly under large enough out-of-plane driving fields. However, κ is totally neglected by using the static width Δ_0 instead of the real complicated breathing one. This simplification holds for not too narrow magnetic central layers with strong PMA. However, for those with relatively weak PMA and shrinking width, the importance of κ increases. This effect manifests itself as the additional factor $(1 + \frac{\kappa}{4})\frac{K_0}{2\pi}$ in our δH_y term.

V. WALKER CURRENT DENSITY ENHANCEMENT

We turn to DW dynamics driven by in-plane currents ($H_z = 0$ and $J_a \neq 0$). In the absence of BDMI, the in-plane Walker current density reads $J_W^0 = \frac{\Delta_0\gamma H_W^0}{|\alpha-\beta|}\frac{eM_s}{\mu_B P}$, which is proportional to κ through H_W^0. For convenience, we define an "absolute current unit" which is free of κ as $J_0 \equiv \frac{\Delta_0\gamma\alpha H_K}{2|\alpha-\beta|}\frac{eM_s}{\mu_B P} = J_W^0/\kappa$. Without $\mathbf{H}_\perp$, the existence condition of steady flow ($\dot{\varphi} = 0$ and $\dot{\Delta} = 0$) changes the first equation in Eq. (5) to

$$\eta\,\text{sgn}(\alpha - \beta)\frac{J_a}{J_W^0} = g(\varphi) \equiv \frac{b}{\kappa}\cos\varphi + \frac{\sin 2\varphi}{\sqrt{1 + \kappa\sin^2\varphi}}. \qquad (19)$$

For fixed b and κ, once $|g(\varphi)|_{max}$ is found for $\varphi \in [0, 2\pi)$, the new Walker current density is then obtained as $J_W = J_W^0|g(\varphi)|_{max}$. Meanwhile, the sign of b is irrelevant to $|g(\varphi)|_{max}$ since $g(b, \varphi) \equiv g(-b, \varphi + \pi)$. We then set $b > 0$ to simplify the analysis. After defining $x \equiv \sin\varphi$ and introducing $\mathscr{G}(x) \equiv [g(\varphi)]^2$, we have $|g(\varphi)|_{max} = \sqrt{|\mathscr{G}(\varphi)|_{max}}$. The extremum condition, $d\mathscr{G}/dx = 0$, can be transformed into a quartic equation of x^2, whose exact solution is too complicated to write out explicitly. Alternatively, by numerically searching for the maximum of $\mathscr{G}(x)$ for $x \in [-1, 1]$, the new Walker current densities J_W in units of J_W^0 and J_0 are, respectively, provided in Figs. 5(a) and 5(b). Meanwhile, the in-plane angle φ_0 where J_W is reached is depicted in Fig. 5(c). Also, the region $\{(\kappa, b): 0.02 \leqslant \kappa \leqslant 2, 0 \leqslant b \leqslant 2\}$ is our parameter space.

Like in the field-driven case, under finite b, J_W/J_W^0 can reach infinity under small enough κ. However, this is just an illusion. In terms of the "κ-free" J_0, the real J_W varies within a finite range. In our parameter space we have $J_W/J_0 \approx b + \kappa$, which manifests itself as the inclined and almost flat plane in Fig. 5(b). This linear behavior also comes from the joint action of the transverse hard anisotropy field and the transverse component of the BDMI effective field. For a fixed finite b, the location φ_0 where J_W is achieved rapidly decreases from $\pi/4$ to 0 as κ shrinks. This is due to the fact that under $\kappa \ll 1$ the first term in Eq. (19) dominates; thus, $g(\varphi)$ achieves the maximum absolute value at $\varphi_0 = 0$.

A special case is $b^2 = 4\kappa$. Now the quartic equation of x^2 (coming from $d\mathscr{G}/dx = 0$) is reduced to a cubic one: $\kappa(x^2)^3 +$
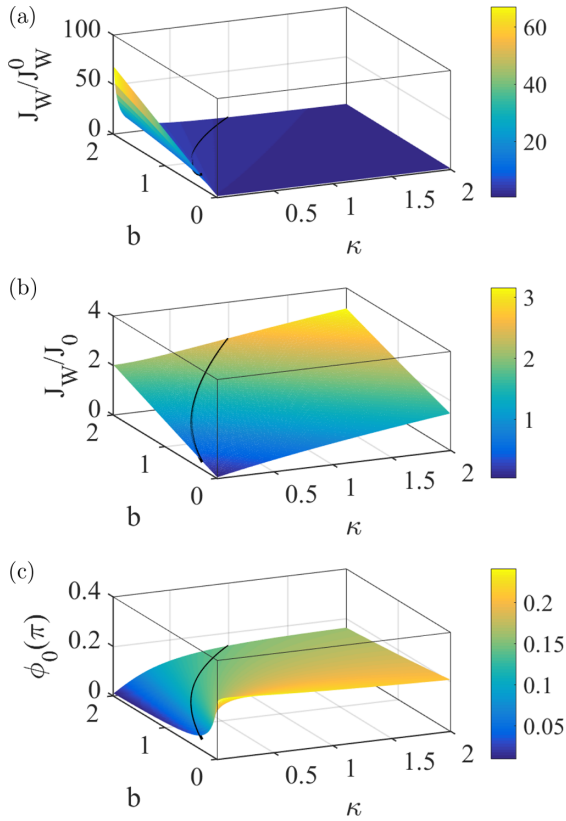
FIG. 5. BDMI-modified Walker current density J_W (a) in units of J_W^0 and (b) in units of J_0 and (c) the corresponding in-plane angle under in-plane driving current $J_a\mathbf{e}_x$. All data come from direct numerical searching on the maxima of the function $\mathscr{G}(x = \sin\varphi)$ in (b, κ) space. The solid curve in (c) comes from $\varphi_0 = \arcsin\tilde{x}$ in Eq. (20), while those in (a) and (b) are, respectively, $\sqrt{\mathscr{G}(\tilde{x})}$ and $\kappa\sqrt{\mathscr{G}(\tilde{x})}$.

$(1 - 2\kappa)(x^2)^2 - (4 + 1/\kappa)x^2 + 1 = 0$. Its solution

$$\tilde{x} = \left[\frac{2\kappa - 1}{3\kappa} + \frac{4(1 + \kappa)}{3\kappa} \cos\frac{\theta + \pi}{3} \right]^{\frac{1}{2}}, \quad \theta = \cos^{-1}\frac{\frac{11}{16} - \kappa}{1 + \kappa}, \tag{20}$$

gives the maxima of $\mathscr{G}(x)$. The resulting Walker current density is $J_W = J_W^0 \sqrt{\mathscr{G}(\tilde{x})}$, which is plotted in Figs. 5(a) and 5(b) by solid curves. The corresponding in-plane angle $\varphi_0 = \arcsin\tilde{x}$ is depicted in Fig. 5(c). The high coincidence between the numerics and analytics of this special case provides strong cross validation for both methods.

Finally, we pay special attention to the $\kappa \ll 1$ case. Now $J_W \approx bJ_0$, meaning that the Walker current density is completely determined by BDMI. Recalling the definitions of J_0 and b, we have

$$J_W = \frac{\alpha}{|\alpha - \beta|} \frac{\pi g_e |D_b|}{2\hbar P}, \tag{21}$$

where g_e is the electron g factor. For $|J_a| \leqslant J_W$, the wall takes the steady-flow mode with velocity $\dot{q} = -\frac{\beta}{\alpha}B_J$. The maximum DW velocity occurs at $J_a = J_W$ and turns out to be

$$u_{\kappa\to 0}^{max} = -\frac{\beta}{|\alpha - \beta|} \frac{\pi\gamma_e |D_b|}{2M_s} = -\frac{\beta}{|\alpha - \beta|} |v_{\kappa\to 0}^{max}|. \tag{22}$$

For a rough estimation, the magnetic parameters are the same as those in field-driven case. In addition, we set $\beta = 0.05$ and $P = 0.3$. Then $J_W \approx 1.59 \times 10^9$ A/cm^2, and $u_{\kappa\to 0}^{max} \approx -276$ m/s. It seems that the Walker current density could be pushed to a relatively high value at which a large wall velocity might be achieved. However, DWs will collapse before $|J_a|$ approaches J_W since it is too high for real MHs. What our theory proves is that in BDMI-MHs, under reasonable in-plane current density (10^7–10^8 A/cm^2) DWs always take steady flows with a velocity of several or tens of meters per second. This comes from the relatively low efficiency of spin-transfer torques from in-plane currents. For the same reason, it does not make much sense to calculate the drifting velocity $\langle\dot{q}\rangle$ under $|J_a| \gg J_W$ and, furthermore, the $\langle\dot{q}\rangle \sim H_\perp$ dependence under large J_a. For the completeness of the analytics, we give these results in Appendix B for reference.

VI. DISCUSSION AND CONCLUSION

First of all, we would like to discuss the differences in the effects of BDMI and IDMI on 180° DWs (180DWs). The effects of BDMI on 180DWs mainly reside in (i) the type selection of static walls, (ii) dynamical boosting in the steady-flow mode, and (iii) Walker limit enhancement. In principle, the bridge linking BDMI energy density to the various final results is the BDMI-induced in-plane transverse effective field. For static 180DWs existing in thin-film-shape MHs without any DMI, generally, they are Néel type. This is due to the fact that Néel-type (Bloch-type) 180DWs have zero (nonzero) surface and nonzero (zero) bulk magnetic charges. The principle of energy minimization requires the existence of as few magnetic charges as possible. For thin-film-shape MHs, the surface effect becomes significant; thus, Néel-type 180DWs dominate. In the presence of IDMI, the IDMI-induced in-plane effective magnetic field is along the long axis of MHs and thus strengthens the Néel-type nature of static 180DWs. However, for BDMI-MHs, the situation is quite different. The BDMI-induced in-plane effective magnetic field is along the transverse direction. For large enough BDMI, the central magnetizations of 180DWs are turned to the transverse direction; thus, 180DWs prefer the Bloch type. The energy gain from the extra surface magnetic charges will be compensated by the energy loss from the BDMI term for the spinning magnetization texture within the wall region. One possible disadvantage of Bloch-type 180DWs comes from the non-negligible "cross talking" between them since a larger magnetic flux (originating from surface magnetic charges) exists outside wall regions. This could limit the integration level of nanodevices based on them. However, large entanglements between these walls become possible. This will provide a new stage for quantum information based on the interactions of spin waves and a series of Bloch-type 180DWs in thin-film-shape MHs. As for dynamical manipulations, the transverse BDMI-induced in-plane effective field can boost the wall velocity in the steady-flow mode in terms of broadening the wall width [51]. In particular, the Walker limit will be enhanced since it is also proportional to wall width. However, for IDMI, none of these effects exist.

Second, we want to address the feasibility of Eq. (4) in this work. In the absence of any DMI, the spatially homogeneous

ϕ in the Walker ansatz has been proven to be a good description of real magnetization distribution. When BDMI emerges, its swirling nature makes θ and ϕ become coupled and entangled everywhere in the MH plane; thus, the theoretical final results can hardly be obtained. Fortunately, for not too strong BDMI, numerical simulations (from OOMMF, MUMAX, etc.) have confirmed that the assumption of spatially homogeneous ϕ is not far from the real magnetization distribution. This is also the choice of nearly all existing theoretical explorations. In particular, the BDMI strength is limited within a relatively weak region in this work ($|b| \leqslant 2$). Therefore, we adopt the assumption of homogeneous ϕ in our present theoretical investigations to provide the "leading-order" physics. Further explorations including the spatially varying ϕ will be our next step in future works. On the other hand, in perfect not-too-narrow strip-shaped MHs, DMIs can induce the wall tiling χ with respect to $+\mathbf{e}_y$ [42]. However, for real MHs with disorders, the walls take a complex meandering shape with the magnetization vectors rotating several times along them and thus show inconspicuous tilting [25,26,52]. This leads to the negligible longitudinal component of $\mathbf{H}_b$ (proportional to $\nabla_y m_z$), hence explaining the feasibility of Eq. (4). Another neglected effect is the magnetization canting θ_∞ [51] in domains by in-plane fields either from intrinsic BDMI or from external exertion. If both χ and θ_∞ are considered, a more complicated wall ansatz

$$\tan\frac{\vartheta}{2} = \frac{e^R + \tan(\theta_\infty/2)}{1 + e^R \tan(\theta_\infty/2)}, \quad \phi = \varphi(t), \quad (23)$$

can be proposed with $R \equiv \eta[(x - q)\cos\chi + y\sin\chi]/\Delta$. By integrating dynamical equations over infinite strip length and finite width, the so-called $q - \varphi - \chi$ [42] or $q - \varphi - \chi - \Delta$ [53,54] models emerge. However, they are too complicated to provide clear physical pictures in analyzing DW dynamics.

Third, in the steady-flow mode the wall width has an explicit expression. In the precessional-flow mode the wall begins to breathe, leading to a time-dependent wall width $\Delta(t)$. The simple approximation in Sec. IV, i.e., $\Delta = \Delta_0(1 + \kappa\sin^2\varphi)^{-1/2}$, is directly borrowed from the steady-flow mode but not the exact solution of $\Delta(t)$. However, in most cases the shape of the walls does not change too much in a full circle ($|\dot{\Delta}/\Delta| \ll 1$). Therefore, it can be regarded as a good approximation of the actual wall width.

Fourth, under sufficiently large out-of-plane fields, DWs take precessional flows. In this work, during a full circle ($0 \leqslant \varphi < 2\pi$) the Taylor expansion is adopted to get a higher-order correction (here the second order). Also, the role of the hard-easy ratio κ is fully revealed, especially in the center offsets of $\langle \dot{q} \rangle[H_y]$ parabolas. This strategy holds under the assumption that magnetic anisotropic, in-plane bias and BDMI effective fields are all small compared with out-of-plane driving fields. Generally, this condition is not hard to achieve and thus makes the corresponding measurements feasible. However, for chiral magnets with sufficiently large BDMI, to achieve the full parabola quite large driving fields have to be exerted, which could make the DW structure unstable. This possibility limits the application of our theories presented above.

Alternatively, in our recent work (see Ref. [45]) another approximation was adopted: for large enough H_z, DWs pre-

cess almost evenly in a full circle. After linearization of trigonometric functions in dynamical equations, the average wall velocity within $\varphi \in [0, 1)$ is used to mimic the one over a full circle. Regarding this approach, we would like to bring up the following comments: (i) The wall width is always taken as the static one, Δ_0, which is κ independent. This may not have much effect in wide MHs; however, in relatively narrow ones the effects of κ could get stronger. (ii) This approach is not subject to the limitation that all other fields should be small compared with out-of-plane driving fields. However, it suffers from the constraint that the analytics can hold only close to the dome summits or canyon bottoms. Therefore, it cannot explain the further evolution of wall velocity when in-plane bias fields move far away from the centers of domes or canyons. (iii) After series expansions, an additional absolute linear term emerges which is the direct consequence of the linearization operation. For example, to compare it with Eqs. (13) and (18) in the present work, the field-driven wall velocity $v_{b,T}$ in Ref. [45] can be expanded as

$$\frac{v_{b,T}}{\eta\alpha\Delta_0\bar{\gamma}H_z} = 1 + \frac{\pi}{4\alpha}|\Gamma| + \frac{\pi^2}{12}|\Gamma|^2, \quad (24)$$

with $\Gamma \equiv \frac{H_y}{H_z} - \eta\frac{H_b^0}{H_z} - \frac{2\kappa}{\pi}\frac{H_K}{H_z}$. Therefore, $v \sim H_\perp$ curves in Ref. [45] are generally not parabolas but cones around dome summits or canyon bottoms. However, since both $(1 + \frac{\kappa}{4})$ and I_4/I_3 approach 1 when $\kappa \to 0$ and H_K/H_z becomes neglectable in not-too-narrow geometries, the correctness of both schemes can be cross verified.

In summary, the effects of BDMI on the static chirality and dynamic behaviors of DWs in strip-shaped BDMI-MHs have been systematically explored. We highlighted the Walker limit enhancements by BDMI since the latter induces an extra transverse field component. Even in BDMI-MHs with small κ, the finite BDMI therein ensures that DWs can acquire sufficiently large steady-flow velocities. This helps DWs break through various blocking mechanisms and become fast carriers of information. In addition, drifting velocities of DWs far beyond Walker breakdown were obtained by series expansions. It turns out that κ has the potential to effectively manipulate DW dynamics in the precessional-flow mode. Our results pave the way for development and performance optimization of future magnetic nanodevices based on BDMI-MHs.

APPENDIX A: MAXIMUM VALUE AND LOCATION OF $|f(\varphi)|$

By setting $x \equiv \sin\varphi$ and defining

$$\mathscr{F}(x) \equiv [f(\varphi)]^2 = (1 - x^2)\left(2x + \frac{b}{\kappa}\sqrt{1 + \kappa x^2}\right)^2, \quad (A1)$$

the searching of maximum $|f(\varphi)|$ for $\varphi \in [0, 2\pi)$ is equivalent to that of $\mathscr{F}(x)$ for $|x| \leqslant 1$. We denote the lo-

cation of maximum as $\tilde{x}$; then $\mathscr{F}(x)|_{\max} = (1 - \tilde{x}^2)(2\tilde{x} + b\sqrt{1 + \kappa\tilde{x}^2}/\kappa)^2$. The maximum of $|f(\varphi)|$ is thus $\sqrt{\mathscr{F}(x)|_{\max}}$ at $\varphi_0 = \sin^{-1}\tilde{x}$. The detailed $\tilde{x}$ is as follows:

(a) When $0 < \kappa \leqslant 1$, (a1) for $0 < b^2 < 4\kappa$,

$$\tilde{x} = \left[\frac{\kappa - 1}{3\kappa} + \frac{|1 - \kappa|}{3\kappa} \sqrt{\frac{\left(\frac{\kappa+2}{1-\kappa}\right)^2 - \frac{b^2}{4\kappa}}{1 - \frac{b^2}{4\kappa}}} \cos\frac{\theta + \pi}{3} \right]^{\frac{1}{2}},$$

$$\theta = \arccos\left\{ \frac{\sqrt{1 - \frac{b^2}{4\kappa}}\left[1 + \frac{b^2}{4\kappa}\left(\frac{1-\kappa}{\kappa+2}\right)^3\right]}{\left[1 - \frac{b^2}{4\kappa}\left(\frac{1-\kappa}{\kappa+2}\right)^2\right]^{3/2}} \right\}; \quad \text{(A2)}$$

(a2) for $b^2 = 4\kappa$,

$$\tilde{x} = \sqrt{\frac{\kappa}{2\kappa + 1}}; \quad \text{(A3)}$$

(a3) for $b^2 > 4\kappa$,

$$\tilde{x} = \sqrt{-\frac{1-\kappa}{3\kappa} - \frac{\sqrt[3]{Y_+} + \sqrt[3]{Y_-}}{3(4\kappa - b^2)}},$$

$$Y_{\pm} = (b^2 - 4\kappa)^2\left\{ \frac{(\kappa+2)^3}{2\kappa^2} + \frac{b^2(1-\kappa)^3}{8\kappa^3} \right.$$

$$\left. \mp \frac{3}{2}\sqrt{\frac{3b^2\left[(\kappa+2)^3 + \frac{b^2}{4\kappa^2}(\kappa+1)(1-\kappa)^3\right]}{\kappa^3(b^2 - 4\kappa)}} \right\}. \quad \text{(A4)}$$

(b) When $\kappa > 1$, (b1) for $0 < b^2 < 4\kappa$, the result is the same as Eq. (A2); (b2) for $b^2 = 4\kappa$, the result is the same as Eq. (A3); (b3) for $4\kappa < b^2 < 4\kappa^2(\kappa+2)^3/[(\kappa+1)(\kappa-1)^3]$, the result is the same as Eq. (A4); (b4) for $b^2 = 4\kappa^2(\kappa+2)^3/[(\kappa+1)(\kappa-1)^3]$,

$$\tilde{x} = \sqrt{\frac{\kappa^2 - 1}{\kappa(2\kappa + 1)}}; \quad \text{(A5)}$$

(b5) for $b^2 > 4\kappa^2(\kappa+2)^3/[(\kappa+1)(\kappa-1)^3]$,

$$\tilde{x} = \left[\frac{\kappa - 1}{3\kappa} + \frac{\kappa - 1}{3\kappa}\sqrt{\frac{1 - \frac{4\kappa}{b^2}\left(\frac{\kappa+2}{\kappa-1}\right)^2}{1 - \frac{4\kappa}{b^2}}}\cos\frac{\theta}{3} \right]^{\frac{1}{2}},$$

$$\theta = \arccos\left\{ -\frac{\sqrt{1 - \frac{4\kappa}{b^2}}\left[1 - \frac{4\kappa}{b^2}\left(\frac{\kappa+2}{\kappa-1}\right)^3\right]}{\left[1 - \frac{4\kappa}{b^2}\left(\frac{\kappa+2}{\kappa-1}\right)^2\right]^{3/2}} \right\}. \quad \text{(A6)}$$

APPENDIX B: CURRENT-DRIVEN DW DYNAMICS UNDER $|J_a| \gg J_W$

In this Appendix, drifting velocities of DWs under high enough in-plane current densities are provided, assuming that they have not collapsed. First, we define several integrals:

$$I_1 = \int_0^{2\pi} \frac{\sin^2 2\varphi}{(1 + \kappa\sin^2\varphi)^{3/2}}d\varphi$$

$$= \frac{16\sqrt{1+\kappa}}{\kappa}\left[\frac{2+\kappa}{\kappa(1+\kappa)}K\left(\sqrt{\frac{\kappa}{1+\kappa}}\right) - \frac{2}{\kappa}E\left(\sqrt{\frac{\kappa}{1+\kappa}}\right) \right],$$

$$I_2 = \int_0^{2\pi} \frac{\sin^2\varphi}{(1 + \kappa\sin^2\varphi)^{3/2}}d\varphi$$

$$= \frac{4}{\kappa\sqrt{1+\kappa}}\left[K\left(\sqrt{\frac{\kappa}{1+\kappa}}\right) - E\left(\sqrt{\frac{\kappa}{1+\kappa}}\right) \right],$$

$$I_3 = \int_0^{2\pi} \frac{\cos^2\varphi}{(1 + \kappa\sin^2\varphi)^{3/2}}d\varphi$$

$$= \frac{4}{\kappa\sqrt{1+\kappa}}\left[(1+\kappa)E\left(\sqrt{\frac{\kappa}{1+\kappa}}\right) - K\left(\sqrt{\frac{\kappa}{1+\kappa}}\right) \right],$$

$$I_4 = \int_0^{2\pi} \frac{\cos^2\varphi}{1 + \kappa\sin^2\varphi}d\varphi = 2\pi\frac{\sqrt{1+\kappa} - 1}{\kappa}, \quad \text{(B1)}$$

where $E(k) \equiv \int_0^{\pi/2} d\omega\sqrt{1 - k^2\sin^2\omega}$ is the complete elliptic integral of the second kind.

When $|J_a|$ exceeds J_W, the steady-flow mode fails, and the wall undergoes precessional flow. The precession period T_0' is

$$T_0' = \frac{1}{\bar{\gamma}H_W^0}\int_0^{2\pi} \frac{d\varphi/\sqrt{1 + \kappa\sin^2\varphi}}{\sigma\frac{J_a}{J_W^0} - \frac{b}{\kappa}\cos\varphi - \frac{\sin 2\varphi}{\sqrt{1+\kappa\sin^2\varphi}}}, \quad \text{(B2)}$$

in which $\sigma \equiv \eta\,\text{sgn}(\alpha - \beta)$ and a prime means the quantity is for the current-driven case. In high-current limit, after preserving the second-order small quantities we have

$$T_0' \approx \frac{\sigma}{\bar{\gamma}H_W^0}\frac{J_W^0}{J_a}\left\{ K_0 + \left[\frac{K_0}{2}\left(\frac{b}{\kappa}\right)^2 + I_1 \right]\left(\frac{J_W^0}{J_a}\right)^2 \right\}. \quad \text{(B3)}$$

Thus, the time-averaged wall velocity is

$$\langle\dot{q}\rangle_0' = -\frac{1 + \alpha\beta}{1 + \alpha^2}B_J + \frac{(\alpha - \beta)B_J}{\alpha(1 + \alpha^2)}\left[\frac{1}{2}\left(\frac{b}{\kappa}\right)^2 + \frac{I_1}{K_0} \right]\left(\frac{J_W^0}{J_a}\right)^2, \quad \text{(B4)}$$

which provides an additional $(J_a)^{-1}$ term.

Next, we turn on $\mathbf{H}_{\perp}$. The Walker current density J_W will inevitably be affected by $\mathbf{H}_{\perp}$, but the exact dependence is hard to obtain. For $J_a \gg J_W$, the rotational period is similar to Eq. (B2) except for an additional $-\frac{\pi H_{\perp}}{H_K}\frac{\sin(\varphi - \phi_{\perp})}{\sqrt{1+\kappa\sin^2\varphi}}$ term in the denominator of the integral kernel.

For longitudinal in-plane bias fields ($H_{\perp} = H_x$ and $\phi_{\perp} = 0$), the new period is

$$T_x' = T_0' + \frac{\sigma I_2}{\bar{\gamma}H_W^0}\left(\frac{\pi H_x}{H_K}\right)^2\left(\frac{J_W^0}{J_a}\right)^3. \quad \text{(B5)}$$

This leads to a new velocity,

$$\langle\dot{q}\rangle'[H_x] = \langle\dot{q}\rangle_0' + \frac{\alpha - \beta}{\alpha(1 + \alpha^2)}\left(\frac{\pi H_x}{H_K}\right)^2\frac{I_2}{K_0}\left(\frac{J_W^0}{J_a}\right)^2 B_J. \quad \text{(B6)}$$

For fixed J_a, the $\langle \dot{q} \rangle' \sim H_x$ curve is a parabola with its center located at $H_x = 0$, and its opening direction depends on the relative strength of α and β.

For transverse in-plane bias fields ($H_\perp = H_y$, $\phi_\perp = \pi/2$), the period becomes

$$T_y' = T_0' + \frac{\sigma}{\bar{\gamma} H_W^0} \left[\left(\frac{\pi H_y}{H_K} \right)^2 I_3 - 2 \frac{\pi H_y}{H_K} \frac{b}{\kappa} I_4 \right] \left(\frac{J_W^0}{J_a} \right)^3 . \quad \text{(B7)}$$

The resulting drifting velocity is then

$$\langle \dot{q} \rangle'[H_y] = \langle \dot{q} \rangle_0' + \frac{\alpha - \beta}{\alpha(1 + \alpha^2)} \left\{ \frac{\pi^2 I_3}{K_0} \left(\frac{H_y - \delta H_y'}{H_K} \right)^2 \right.$$
$$\left. - \left(\frac{b}{\kappa} \right)^2 \frac{(I_4)^2}{K_0 I_3} \right\} \left(\frac{J_W^0}{J_a} \right)^2 B_J , \quad \text{(B8)}$$

with $\delta H_y' = \eta(I_4/I_3) H_b^0$. Now the $\langle \dot{q} \rangle' \sim H_y$ curve becomes a parabola whose center is located at $H_y = \delta H_y'$ and whose opening direction depends on $\text{sgn}(\alpha - \beta)$.

[1] M. Heide, G. Bihlmayer, and S. Blügel, Phys. Rev. B **78**, 140403(R) (2008).

[2] A. Thiaville, S. Rohart, E. Jué, V. Cros, and A. Fert, Europhys. Lett. **100**, 57002 (2012).

[3] G. Chen, J. Zhu, A. Quesada, J. Li, A. T. N'Diaye, Y. Huo, T. P. Ma, Y. Chen, H. Y. Kwon, C. Won, Z. Q. Qiu, A. K. Schmid, and Y. Z. Wu, Phys. Rev. Lett. **110**, 177204 (2013).

[4] G. Chen, S. P. Kang, C. Ophus, A. T. N'Diaye, H. Y. Kwon, R. T. Qiu, C. Won, K. Liu, Y. Wu, and A. K. Schmid, Nat. Commun. **8**, 15302 (2017).

[5] V. Risinggård and J. Linder, Phys. Rev. B **95**, 134423 (2017).

[6] M. Li, J. Wang, and J. Lu, New J. Phys. **21**, 053011 (2019).

[7] S. Mühlbauer, B. Binz, F. Jonietz, C. Pfleiderer, A. Rosch, A. Neubauer, R. Georgii, and P. Böni, Science **323**, 915 (2009).

[8] X. Z. Yu, Y. Onose, N. Kanazawa, J. H. Park, J. H. Han, Y. Matsui, N. Nagaosa, and Y. Tokura, Nature (London) **465**, 901 (2010).

[9] W. Jiang, G. Chen, K. Liu, J. Zang, S. G. te Velthuis, and A. Hoffmann, Phys. Rep. **704**, 1 (2017).

[10] J. Chen, L. Wang, M. Zhang, L. Zhou, R. Zhang, L. Jin, X. Wang, H. Qin, Y. Qiu, J. Mei, F. Ye, B. Xi, H. He, B. Li, and G. Wang, Nano Lett. **19**, 6144 (2019).

[11] X. Zhang, Y. Zhou, K. M. Song, T.-E. Park, J. Xia, M. Ezawa, X. Liu, W. Zhao, G. Zhao, and S. Woo, J. Phys.: Condens. Matter **32**, 143001 (2020).

[12] Z. Wang, H. Y. Yuan, Y. Cao, Z.-X. Li, R. A. Duine, and P. Yan, Phys. Rev. Lett. **127**, 037202 (2021).

[13] M. Ezawa, Phys. Rev. B **83**, 100408(R) (2011).

[14] S.-Z. Lin, A. Saxena, and C. D. Batista, Phys. Rev. B **91**, 224407 (2015).

[15] B. Göbel, A. Mook, J. Henk, I. Mertig, and O. A. Tretiakov, Phys. Rev. B **99**, 060407(R) (2019).

[16] L. Shen, J. Xia, X. Zhang, M. Ezawa, O. A. Tretiakov, X. Liu, G. Zhao, and Y. Zhou, Phys. Rev. Lett. **124**, 037202 (2020).

[17] X. Zhang, J. Xia, L. Shen, M. Ezawa, O. A. Tretiakov, G. Zhao, X. Liu, and Y. Zhou, Phys. Rev. B **101**, 144435 (2020).

[18] I. Dzyaloshinsky, J. Phys. Chem. Solids **4**, 241 (1958).

[19] T. Moriya, Phys. Rev. **120**, 91 (1960).

[20] M. Bode, M. Heide, K. von Bergmann, P. Ferriani, S. Heinze, G. Bihlmayer, A. Kubetzka, O. Pietzsch, S. Blügel, and R. Wiesendanger, Nature (London) **447**, 190 (2007).

[21] S. X. Huang and C. L. Chien, Phys. Rev. Lett. **108**, 267201 (2012).

[22] O. Meshcheriakova, S. Chadov, A. K. Nayak, U. K. Rößler, J. Kübler, G. André, A. A. Tsirlin, J. Kiss, S. Hausdorf, A. Kalache, W. Schnelle, M. Nicklas, and C. Felser, Phys. Rev. Lett. **113**, 087203 (2014).

[23] S. Singh, S. W. D'Souza, J. Nayak, E. Suard, L. Chapon, A. Senyshyn, V. Petricek, Y. Skourski, M. Nicklas, C. Felser *et al.*, Nat. Commun. **7**, 12671 (2016).

[24] M. Vaňatka, J.-C. Rojas-Sánchez, J. Vogel, M. Bonfim, M. Belmeguenai, Y. Roussigné, A. Stashkevich, A. Thiaville, and S. Pizzini, J. Phys.: Condens. Matter **27**, 326002 (2015).

[25] E. Jué, A. Thiaville, S. Pizzini, J. Miltat, J. Sampaio, L. D. Buda-Prejbeanu, S. Rohart, J. Vogel, M. Bonfim, O. Boulle, S. Auffret, I. M. Miron, and G. Gaudin, Phys. Rev. B **93**, 014403 (2016).

[26] T. H. Pham, J. Vogel, J. Sampaio, M. Vaňatka, J.-C. Rojas-Sánchez, M. Bonfim, D. S. Chaves, F. Choueikani, P. Ohresser, E. Otero *et al.*, Europhys. Lett. **113**, 67001 (2016).

[27] F. Ajejas, V. Křižáková, D. de Souza Chaves, J. Vogel, P. Perna, R. Guerrero, A. Gudin, J. Camarero, and S. Pizzini, Appl. Phys. Lett. **111**, 202402 (2017).

[28] D. S. Chaves, F. Ajejas, V. Křižáková, J. Vogel, and S. Pizzini, Phys. Rev. B **99**, 144404 (2019).

[29] Y. H. Choi, Y. Yoshimura, K.-J. Kim, K. Lee, T. W. Kim, T. Ono, C.-Y. You, and M. H. Jung, Sci. Rep. **6**, 23933 (2016).

[30] F. Ajejas, A. Gudín, R. Guerrero, A. A. Barcelona, J. M. Diez, L. de Melo Costa, P. Olleros, M. A. Niño, S. Pizzini, J. Vogel *et al.*, Nano Lett. **18**, 5364 (2018).

[31] A. Hrabec, V. Křižáková, S. Pizzini, J. Sampaio, A. Thiaville, S. Rohart, and J. Vogel, Phys. Rev. Lett. **120**, 227204 (2018).

[32] T. Dohi, S. DuttaGupta, S. Fukami, and H. Ohno, Appl. Phys. Lett. **114**, 042405 (2019).

[33] D.-H. Kim, D.-Y. Kim, S.-C. Yoo, B.-C. Min, and S.-B. Choe, Phys. Rev. B **99**, 134401 (2019).

[34] S. DuttaGupta, S. Fukami, C. Zhang, H. Sato, M. Yamanouchi, F. Matsukura, and H. Ohno, Nat. Phys. **12**, 333 (2016).

[35] P. C. Filippou, J. Jeong, Y. Ferrante, S.-H. Yang, T. Topuria, M. G. Samant, and S. S. P. Parkin, Nat. Commun. **9**, 4653 (2018).

[36] G. V. Karnad, F. Freimuth, E. Martinez, R. Lo Conte, G. Gubbiotti, T. Schulz, S. Senz, B. Ocker, Y. Mokrousov, and M. Kläui, Phys. Rev. Lett. **121**, 147203 (2018).

[37] A. Hrabec, K. Shahbazi, T. A. Moore, E. Martinez, and C. H. Marrows, Nanotechnology **30**, 234003 (2019).

[38] D. Lau and V. Sokalski, AIP Adv. **9**, 035208 (2019).

[39] P.-B. He, M.-Q. Cai, and Z.-D. Li, Phys. Rev. B **102**, 224419 (2020).

[40] Z.-X. Li, Y. Cao, and P. Yan, Phys. Rep. **915**, 1 (2021).

[41] P. Bak and M. H. Jensen, J. Phys. C **13**, L881 (1980).

[42] O. Boulle, S. Rohart, L. D. Buda-Prejbeanu, E. Jué, I. M. Miron, S. Pizzini, J. Vogel, G. Gaudin, and A. Thiaville, Phys. Rev. Lett. **111**, 217203 (2013).

[43] P.-B. He, Eur. Phys. J. B **86**, 412 (2013).

[44] M. Li, Z. An, and J. Lu, Phys. Rev. B **100**, 064406 (2019).

[45] J. Lu, M. Li, and X. R. Wang, Phys. Rev. B **101**, 134431 (2020).

[46] M. Li and J. Lu, J. Magn. Magn. Mater. **525**, 167684 (2021).

[47] J. Du, M. Li, and J. Lu, Phys. Rev. B **103**, 144429 (2021).

[48] J. C. Slonczewski, in *Magnetism And Magnetic Materials — 1971, Parts 1 and 2*, AIP Conf. Proc. No. 5 (AIP, New York, 1972), p. 170.

[49] A. Thiaville, Y. Nakatani, J. Miltat, and Y. Suzuki, Europhys. Lett. **69**, 990 (2005).

[50] X. R. Wang, P. Yan, and J. Lu, Europhys. Lett. **86**, 67001 (2009).

[51] J. Lu, Phys. Rev. B **93**, 224406 (2016).

[52] K. Shahbazi, A. Hrabec, S. Moretti, M. B. Ward, T. A. Moore, V. Jeudy, E. Martinez, and C. H. Marrows, Phys. Rev. B **98**, 214413 (2018).

[53] S. A. Nasseri, S. Moretti, E. Martinez, C. Serpico, and G. Durin, J. Magn. Magn. Mater. **426**, 195 (2017).

[54] S. A. Nasseri, E. Martinez, and G. Durin, J. Magn. Magn. Mater. **468**, 25 (2018).